THE ASTROPHYSICAL JOURNAL, 458:561–575, 1996 February 20

A LARGE-SCALE CO SURVEY TOWARD W3, W4, AND W5

SETH W. DIGEL,[1,2] DAVID A. LYDER,[3] AMY J. PHILBRICK,[1] DANIEL PUCHE,[1] AND PATRICK THADDEUS[1]
Received 1995 April 24; accepted 1995 August 25

ABSTRACT

A CO $J = 1$–0 survey of the outer Galaxy toward W3, W4, and W5 is described. The bright molecular emission in the W3 region in the Perseus arm is prominent, and little emission is seen at greater Galactocentric distances. The extensive local emission in the survey contains the large molecular cloud complex associated with Cam OB1. Between the local and Perseus arm emission, a nearly empty gap in velocity is seen across the entire longitude range. On the assumptions that the kinematically derived width of the gap is the true width and that the X ratio is constant, the arm-interarm contrast of CO is $\geq 25{:}1$ in surface density. A few clouds are detected beyond the Perseus arm, and only one cloud, already known, is detected at extreme Galactocentric distances, beyond the Perseus and outer arms. The cumulative mass distribution of the clouds in the Perseus arm has power-law index 0.65 ± 0.15, and the clouds there are systematically less luminous in CO by a factor 3.5 ± 2 than clouds near the solar circle. The distribution of molecular gas with Galactocentric distance in the outer Galaxy is compared with that of luminous *Infrared Astronomy Satellite* point sources that trace massive star-forming regions. The agreement is generally good, with evidence for enhanced star formation relative to the surface density of molecular gas in the W3 region and perhaps also in the outer arm.

Subject headings: Galaxy: structure — ISM: clouds — ISM: individual (W3, W4, W5) — ISM: molecules — radio lines: ISM

1. INTRODUCTION

A survey of the CO $J = 1$–0 line, the most widely used tracer of interstellar molecular gas, toward the extensive molecular complexes associated with W3, W4, and W5 (hereafter referred to as the "W3 region") was undertaken with the Harvard-Smithsonian Center for Astrophysics 1.2 m telescope as part of a general CO survey of the second quadrant. The region $131° \leq l \leq 144°$, $-2° \leq b \leq +4°$, with an extension to $b = +8°$ on $139° \leq l \leq 144°$, was chosen because it contains one of the largest molecular associations in the Perseus arm, as well as a number of supernova remnants, young H II regions, and newly formed complexes of massive stars. A rich collection of local objects also lies in this direction, including a tangle of molecular clouds related to young and old H II regions and the stellar association Cam OB1. This longitude range is well suited for study of the outer Galaxy, having a number of unobscured lines of sight to the Perseus arm as well as good kinematic distance discrimination by radial velocities. Earlier surveys of the large-scale (10 pc to 1 kpc) distribution of molecular gas in the region considered here were of lower sensitivity and incompletely sampled (e.g., Lada et al. 1978; Cohen et al. 1980; Thronson, Lada, & Hewagama 1985; Dame et al. 1987).

The present CO survey of the W3 region permits the investigation of the properties of molecular clouds in an ~ 1 kpc segment of the Perseus arm, and the wide latitude range of the survey provides good coverage of the warp and flare of the outer disk. Calibration of the masses of the molecular clouds observed in the Perseus arm and the determination of the arm-interarm contrast, most readily studied in the outer Galaxy, are the principal subjects investigated here. Existing, extensive studies of Population I objects in the region provide a ready database for comparison with the molecular gas; detailed comparison of the observations with star-forming regions will be presented elsewhere (Lyder 1996). The methods of observation and data reduction for the survey are presented in § 2. Maps derived from the survey and findings on the properties of molecular clouds and the distribution of molecular gas are presented in § 3.

[1] Harvard-Smithsonian Center for Astrophysics, MS 72, 60 Garden Street, Cambridge, MA 02138.
[2] NASA Goddard Space Flight Center, Code 631, Greenbelt, MD 20771.
[3] Dominion Radio Astrophysical Observatory, Herzberg Institute of Astrophysics, National Research Council, P.O. Box 248, Penticton, BC V2A 6K3, Canada.

2. OBSERVATIONS & DATA REDUCTION

The 1.2 m millimeter-wave telescope at the Center for Astrophysics (CfA) was used to carry out the survey during the period 1992 November through 1993 March. The telescope is described in detail by Cohen, Dame, & Thaddeus (1986), and its sensitive SIS receiver is described by Leung & Thaddeus (1992). The single-sideband noise temperature of the receiver was typically 65 K, and total powers referred to above the atmosphere were 350–400 K, depending on weather and elevation. At the 115 GHz frequency of the CO 1–0 line, the half-power beamwidth is 8.′7, and the main-beam efficiency is 0.82 (Bronfman et al. 1988). An optical telescope aligned with the axis of the main reflector was used at the beginning of the observing season to establish pointing corrections from observations of ~ 50 stars. The residual pointing errors were found to be 24″ rms, only 5% of the beam size. The stability of the pointing was checked several times during the observing season by continuum scans of the limb of the Sun.

Table 1 summarizes the parameters of the survey. The observations were made on a uniform 3.′75 grid over the indicated ranges of l and b, for a total area of ~ 98 deg^2. Spectra were taken by position switching against two reference directions with a period of 10–20 s, for an rms noise level of 0.29 K in T_{mb} in each 250 kHz (0.65 km s^{-1}) channel. For each spectrum, the total integration time on and off-source was typically 30–40 s. The reference positions (Table 2) were verified by frequency switching to be free of CO emission to a level of 0.07 K rms per channel; two were chosen for each observation to straddle the on-source position in elevation. The partitioning

TABLE 1

PARAMETERS OF THE SURVEY

Parameter	Value
Observing mode	Position switching
Spatial coverage	$131° \leq l \leq 139°$; $-2° \leq b \leq +4°$
	$139° \leq l \leq 144°$; $-2° < b \leq +8°$
Beamwidth (FWHM)	8.7
Sampling interval	Δl, Δb: 3.75
Total number of spectra	25,248
Velocity coverage (LSR)	-133 to $+33$ km s^{-1}
Velocity resolution	0.65 km s^{-1}
Sensitivity per channel	$T_{mb} = 0.29$ K

TABLE 2

REFERENCE POSITIONS

l	b	l	b
131.0	−3.0	137.0	−3.0
132.0	−3.0	137.5	3.0
134.0	−5.0	138.0	−3.0
134.5	2.5	139.0	−5.0
135.0	−5.0	142.0	6.0
135.0	3.0	143.0	6.0
136.0	−5.0	144.0	−3.0
136.5	3.0	145.0	2.0

of the off-source time between the two reference positions was chosen to minimize the offset of the baseline level from 0 K in the net on-off source spectrum. This standard technique with the 1.2 m telescope minimizes the influence of any nonideal behavior of the square-law detectors in the backend. At the beginning of each 6 hr observing session, and more often when the weather was changing, the opacity of water vapor was determined by antenna tipping. No observations were attempted when the zenith optical depth of water was greater than 0.25. The CO peaks toward NGC 7538 and W3 were observed each session to check for variations of the intensity calibration; the integrated antenna temperature for these observations did not vary by more than 5% during the season. Line intensities were calibrated using the standard blackbody chopper wheel technique (Kutner & Ulich 1981).

Except for the recent addition of a wide-bandwidth filter bank, the spectrometer was much as described by Cohen et al. (1986). During the observations here, it consisted of two 256 channel filter banks centered at the same frequency and running in parallel. One has 250 kHz (0.65 km s^{-1}) channels for an overall velocity width of 166 km s^{-1} at 115 GHz, and the other has 500 kHz channels for a width of 332 km s^{-1}. Because the emission detected in this survey all fell within the range of the 250 kHz filter bank, the 500 kHz spectra were used mainly for baseline fitting.

After linear baselines were subtracted, automatic processing was used to identify bad spectra. Visual inspection of a sample of 1000 spectra indicated that the most common residual baseline fluctuation was a low-level ripple with a frequency width of approximately 20 MHz, representing a standing wave not completely canceled by the position switching. Because the amplitude of this ripple was never greater than the rms noise level, groups of 20 adjacent channels, spaced every 10 channels, were averaged together to find significant deviations of the baseline level from zero intensity. Only channels in the 250 kHz filter bank that are believed to be emission free, generally those in the local standard of rest velocity range -130 km s^{-1} $< V_{LSR} < -70$ km s^{-1} were examined. This automatic procedure flagged approximately 4% of the spectra, which were reobserved. Most of the spectra with 20 MHz ripple were taken during periods of changing weather or when the reference positions were unfavorably situated, requiring unusually large switching offsets in elevation.

Line intensities are given here in units of main-beam brightness temperature (T_{mb}), i.e., antenna temperature corrected for atmospheric absorption and main-beam efficiency. Bronfman et al. (1988) determined that the reported intensities of the CfA 1.2 m telescope (then at Columbia University) were ~20% below the true main-beam temperature. Here we adopt the corrected temperature scale of Bronfman et al. (1988). The Columbia CO surveys on the prior scale were used to calibrate the relation between $N(H_2)$ and integrated intensity of CO in the study by Strong et al. (1988) of diffuse gamma-ray emission from the Galaxy. The adjustment to the temperature scale of our survey does not affect derived column densities of H_2; the $N(H_2)/W_{CO}$ ratio of Strong et al. (1988) must be decreased by a compensating factor of 1.2. In order to enhance the signal-to-noise ratio in each spectrum, spatial smoothing of the data cube was done with a Gaussian smoothing function symmetric in l and b with a full width at half-maximum (FWHM) of 4.9 to yield an effective angular resolution of 10′. The rms sensitivity per channel in the smoothed cube is 0.14 K per beam; all results and maps presented here are derived from this smoothed data cube.

3. RESULTS & DISCUSSION

The maps presented in this paper are calculated using a masked moment analysis similar to that described by Adler et al. (1992). In general, large integration ranges in velocity, longitude, or latitude are required to produce maps that adequately summarize the observations, and many emission-free channels are summed in the integration, which degrades the signal-to-noise ratio in the maps. To reduce such degradation, the masked moment method specifies that a threshold test be applied to a smoothed version of the data cube to determine which channels are included in an integration. We have used a threshold of 2 σ for each channel after boxcar smoothing by three channels in velocity and to ~20′ resolution spatially. Drawbacks of this masking are that the number of channels included in a sum varies from position to position, and as Adler et al. (1992) emphasize, standard Gaussian noise statistics no longer apply to the integrated maps. However, the moment analysis very effectively reveals faint emission features over large integration ranges, in the present case suppressing the noise level by a factor of a few. The emission-weighted mean velocity maps presented here are the first-order moments of velocity calculated using the masked moment method.

3.1. *Large-Scale Distribution of* CO

The distribution with velocity of the CO emission for $b = -2°$ to $+4°$ is summarized in the longitude-velocity and latitude-velocity diagrams in Figure 1. Three velocity components are apparent. Emission in the range $V_{LSR} = -60$ km s^{-1} to -30 km s^{-1} is from molecular clouds in the Perseus arm. Relatively nearby foreground CO emission is bifurcated into two fairly well defined lanes which we will call "Cam OB1" (-20 km s^{-1} to -5 km s^{-1}) and "local" (-5 km s^{-1} to $+10$ km s^{-1}). These lanes of nearby clouds are considered

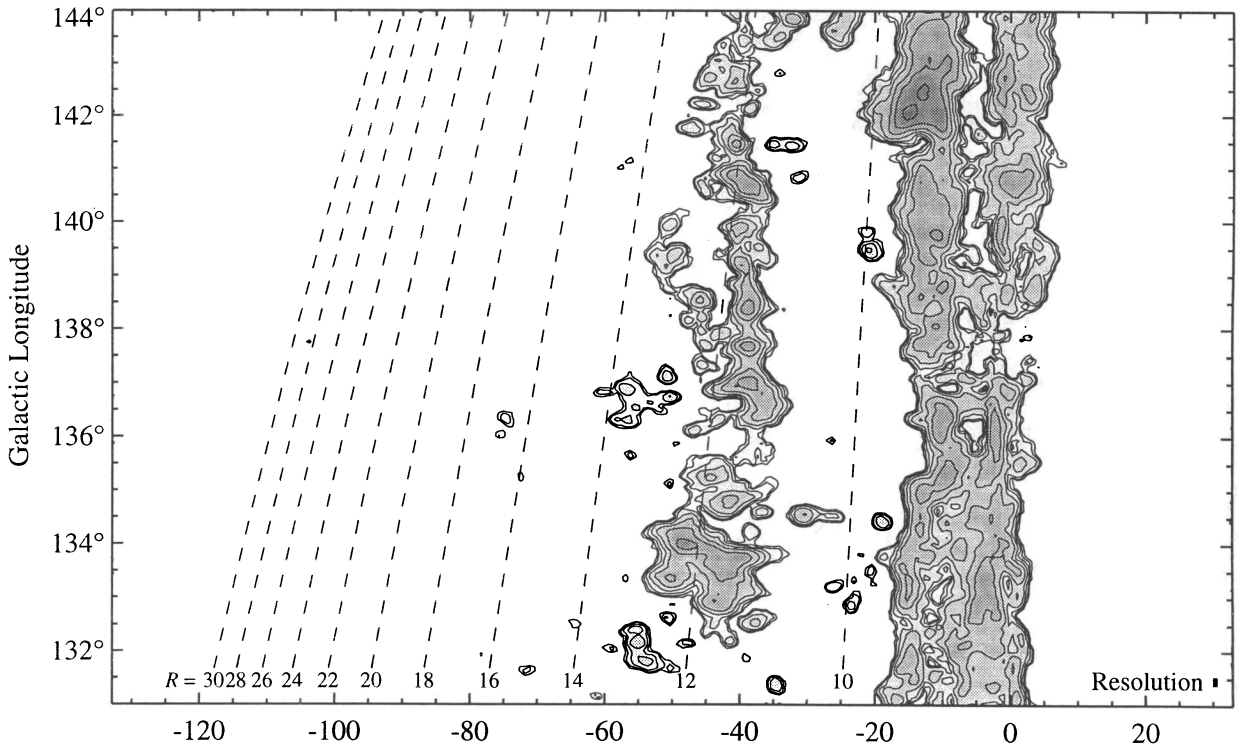

FIG. 1*a*

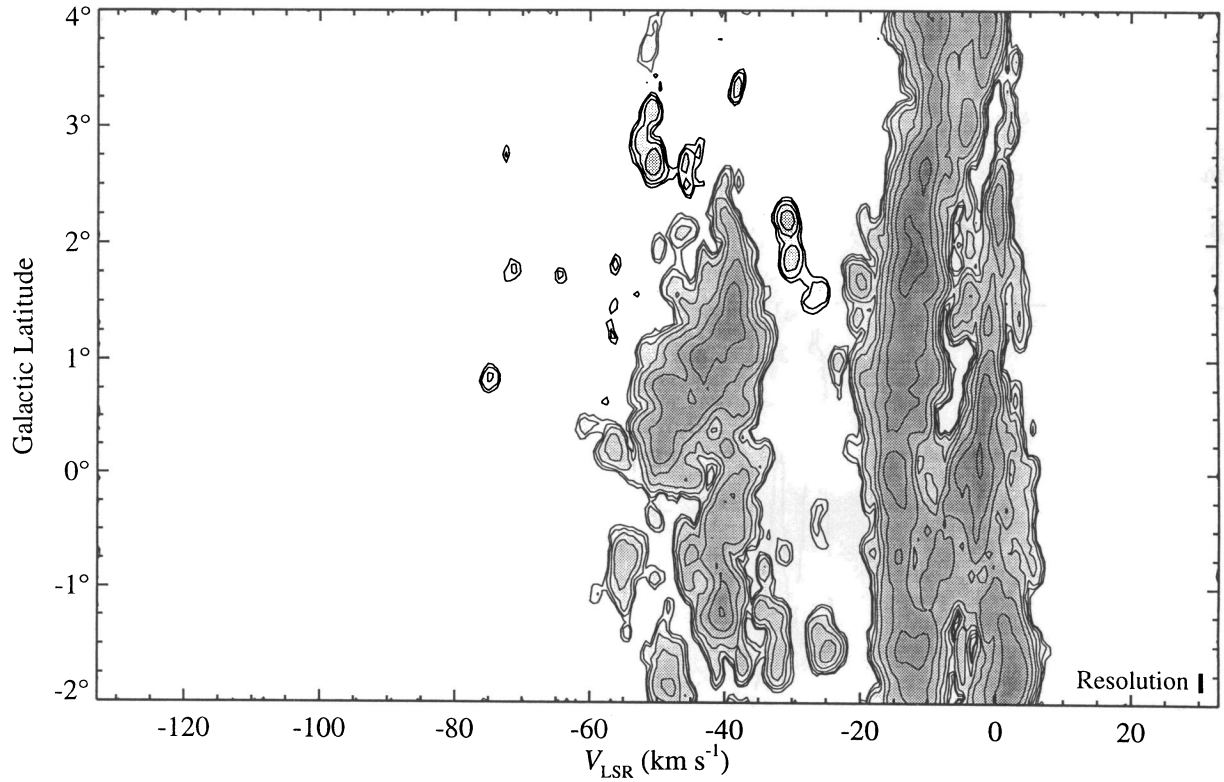

FIG. 1*b*

FIG. 1.—(*a*) Longitude-velocity diagram for the survey, integrated over latitudes $b = -2°$ to $+4°$. Contours are 0.05, 0.1, 0.2, ... K deg. Also shown are lines of constant Galactocentric distance (labeled in kpc) calculated under the assumption of flat rotation curve with $R_\odot = 8.5$ kpc and $V_\odot = 220$ km s^{-1}. (*b*) Latitude-velocity diagram for the survey, integrated over longitudes 131°–144°. Contours are 0.05, 0.1, 0.2, ... K deg. Both maps are calculated using the moment method described in the text to suppress noise.

separately below because they are apparently well separated in distance, containing Cam OB1 at ~800 pc (Haug 1970; Humphreys 1978) and local clouds that are probably coincident with zones of extinction at 200–300 pc first identified by Heeschen (1951). If the two lanes of emission are actually ~500 pc apart, their ~15 km s^{-1} velocity separation may be evidence of a common origin ~3×10^7 yr ago. The local, Cam OB1, and W3 velocity ranges are indicated in Figure 2, which is the average spectrum for the entire survey.

Figures 3–5 contain maps of the emission-weighted mean velocity of CO for the local, Cam OB1, and Perseus arm velocity ranges. The velocity separation of the local and Cam OB1 emission seems to also correspond to spatial separation: the gas in the two velocity ranges overlaps little in l and b, especially at higher longitudes. Also of note in these figures are the large velocity gradients within apparently continuous features in the corresponding spatial maps. For example, the local molecular cloud complex centered near $l, b = 141°, -1°$ (Fig. 3*a*) has a velocity shift of ~5 km s^{-1} between its northern and southern edges (Fig. 3*b*). In the Cam OB1 region, the main complex centered on $l \sim 142°$, $b \sim +2°$ has a velocity gradient of more than 10 km s^{-1} from its southern edge to its center (Fig. 4). In the W3 region, the apparently continuous filament that extends from $l = 134°$ to 137°, $b \sim 0°$ (Fig. 5*a*) is seen in Figure 5*b* to be discontinuous in velocity. The molecular cloud complex associated with W3 (l, $b \sim 133.°5, 0.°8$) has a strong velocity gradient, amounting to ~10 km s^{-1} across its face, as previously noted by Lada et al. (1978).

3.1.1. *Local and Cam OB1 Emission*

The CO emission in the local velocity range is continuous in longitude, except for a break at $l = 138°$, near $b = 0°$ (Fig. 3*a*). No H II regions are known to be associated with the local emission, although the enhancement at $l, b = 135°, -0.°2$ may be related to several Lynd's nebulae: LDN 1363, 1370, and 1365, and LBN 656 and 657.

The dominant complex in the Cam OB1 velocity range is that associated with the Cam OB1 association, e.g. HD 21389 (Lada & Blitz 1988; Fig. 4*a*). This rich complex contains the energetic outflow RAFGL 490 (Snell et al. 1984; Campbell, Persson, & McGregor 1986) and the H II regions S202 (Brand & Blitz 1993), BFS 28, and BFS 29 (Blitz, Fich, & Stark 1982). BFS 24 (Blitz et al. 1982) lies at a lower longitude in this velocity range (Fig. 4*a*). The distances of the H II regions have been determined kinematically from CO radial velocity measurements on the assumption of a flat rotation curve with $R_\odot = 8.5$ kpc and $V_\odot = 220$ km s^{-1}.

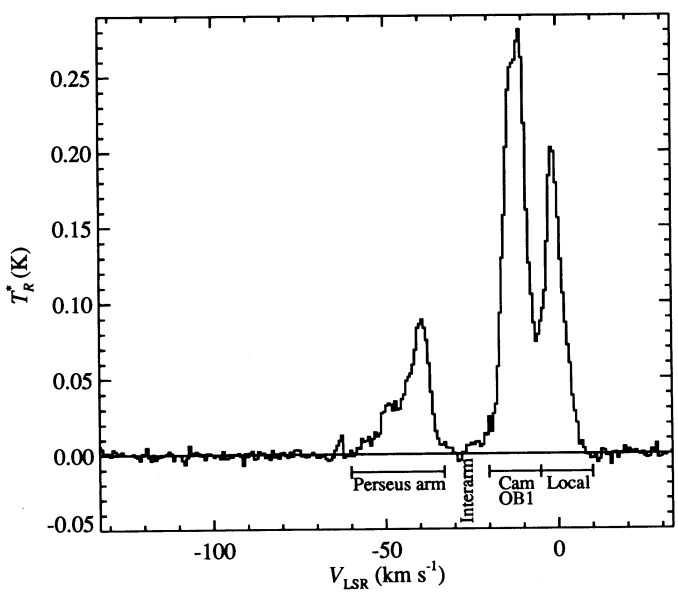

FIG. 2.—Average spectrum of the entire data set.

3.1.2. *Perseus Arm*

The molecular clouds associated with W3, W4, and W5 (Fig. 6) are the most prominent complexes in the Perseus arm in our survey. Associated with W3 is the bright cloud complex centered on $l, b = 133.°5, +1.°0$; with W4, the arclike feature centered on $l, b = 135.°0, -0.°5$; and with W5, the extended feature centered on $l, b = 137.°5, +1.°5$ (Fig. 6). The positions of other H II regions known to be in the Perseus arm are also shown in Figure 6. Their distances have been determined from CO or radio radial velocity measurements (Blitz et al. 1982; Lockman 1989). The greater sensitivity and resolution of the present survey relative to that of Lada et al. (1978) reveal a wealth of underlying, low surface brightness emission. The molecular complexes outline the H II regions, indicated in Figure 6 by their emission in the *Infrared Astronomy Satellite* (*IRAS*) 60 μm band.

3.1.3. *Outer Arm and the Far Outer Galaxy*

The surface density of molecular gas decreases sharply beyond the Perseus arm, and very few clouds are known beyond $R \sim 18$ kpc (Wouterloot et al. 1990). Digel, de Geus, & Thaddeus (1994) searched for the CO emission of distant molecular clouds in the disk of the Galaxy by surveying small regions near shallow peaks of H I column density in the Maryland-Green Bank survey (Westerhout & Wendlant 1982) at large kinematic distance from the Galactic center. The completeness of their study is unknown because only a small fraction of the sky near the Galactic plane was covered. The large-scale survey presented here has sufficient sensitivity and resolution to detect most of the CO clouds cataloged by Digel et al. (1994). One of their clouds, the brightest and most distant ($R = 28$ kpc), cloud 2 at $l, b = 137.°75, -1.°0$, happens to fall within the boundary of our survey.

We searched for distant clouds throughout the survey area. The moment map, such as described above, for the emission in the velocity range -132 km s$^{-1} < V_{LSR} < -60$ km s^{-1} is shown in Figure 7. The clouds are labeled with their emission-weighted mean velocities (in km s^{-1}); most are also apparent in the longitude-velocity diagram (Fig. 1*a*). Several are near -60 km s^{-1} and may be within the outer fringes of the Perseus arm, but a few lie in the kinematic Galactocentric distance range $R = 16$–18 kpc (-85 km s$^{-1} < V_{LSR} < -70$ km s^{-1}) and are likely to be part of the outer arm, as traced by H I (e.g., Henderson, Jackson, & Kerr 1982). The one cloud detected beyond this velocity range is cloud 2, with $V_{LSR} \sim -104$ km s^{-1}. Therefore, the survey of Digel et al. (1994) seems to be fairly complete at the present sensitivity, and their search strategy, concentrating on molecular gas near the peaks of the low contrast ripples in the H I distribution, appears to have been the best to follow short of complete angular coverage. The present sensitivity is sufficient to reveal 250 $M_\odot$, 15 pc diameter molecular clouds at a distance of 5 kpc and 1×10^3 $M_\odot$, 30 pc diameter clouds at 10 kpc, on the assumption of the standard X ratio (see § 3.2).

Several of the distant clouds we detect are 2° or more from

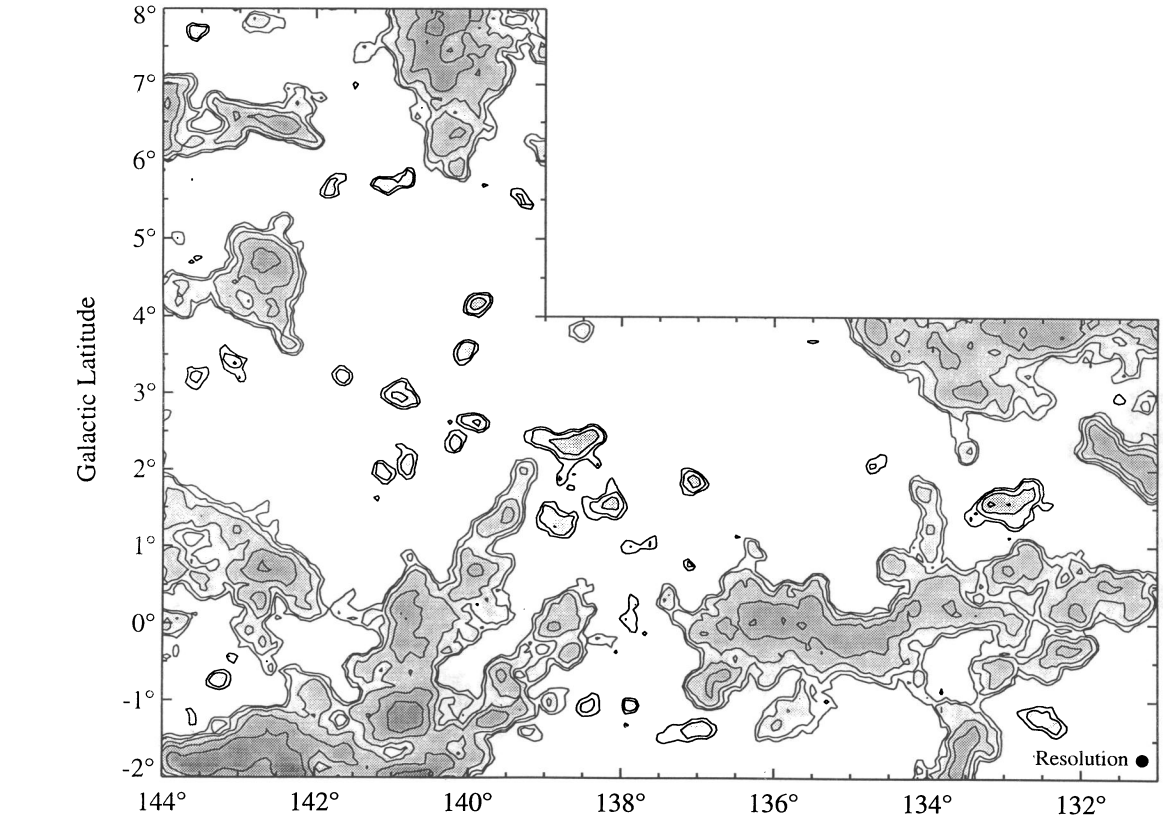

FIG. 3*a*

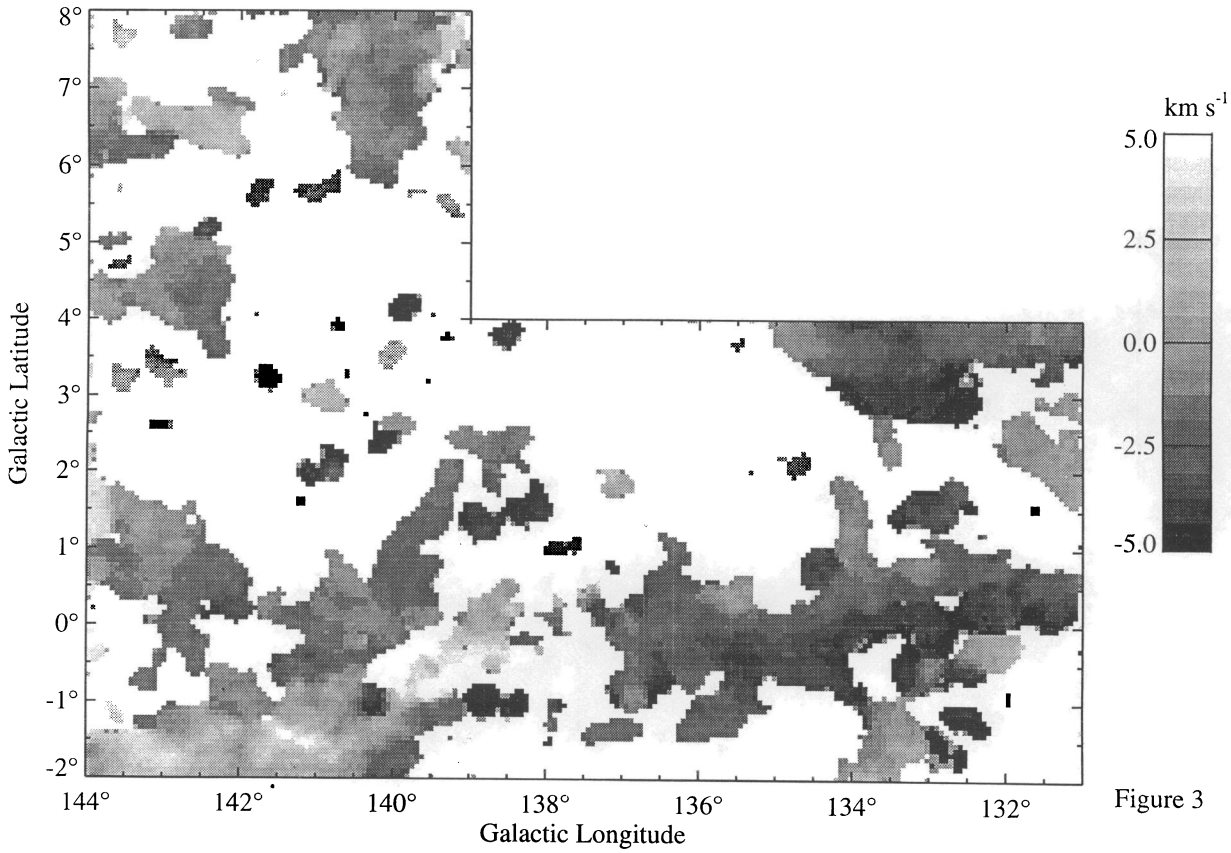

Figure 3

FIG. 3*b*

FIG. 3.—(*a*) Spatial map of the local CO emission, integrated over the range $-5 \leq V_{LSR} \leq +10$ km s^{-1}. Contours are 0.5, 1, 2, ... K km s^{-1}. (*b*) Emission-weighted mean velocity of the CO emission for the same velocity range. The gray-scale representation of velocity covers $-5 \leq V_{LSR} \leq +5$ km s^{-1}, which contains most of the emission.

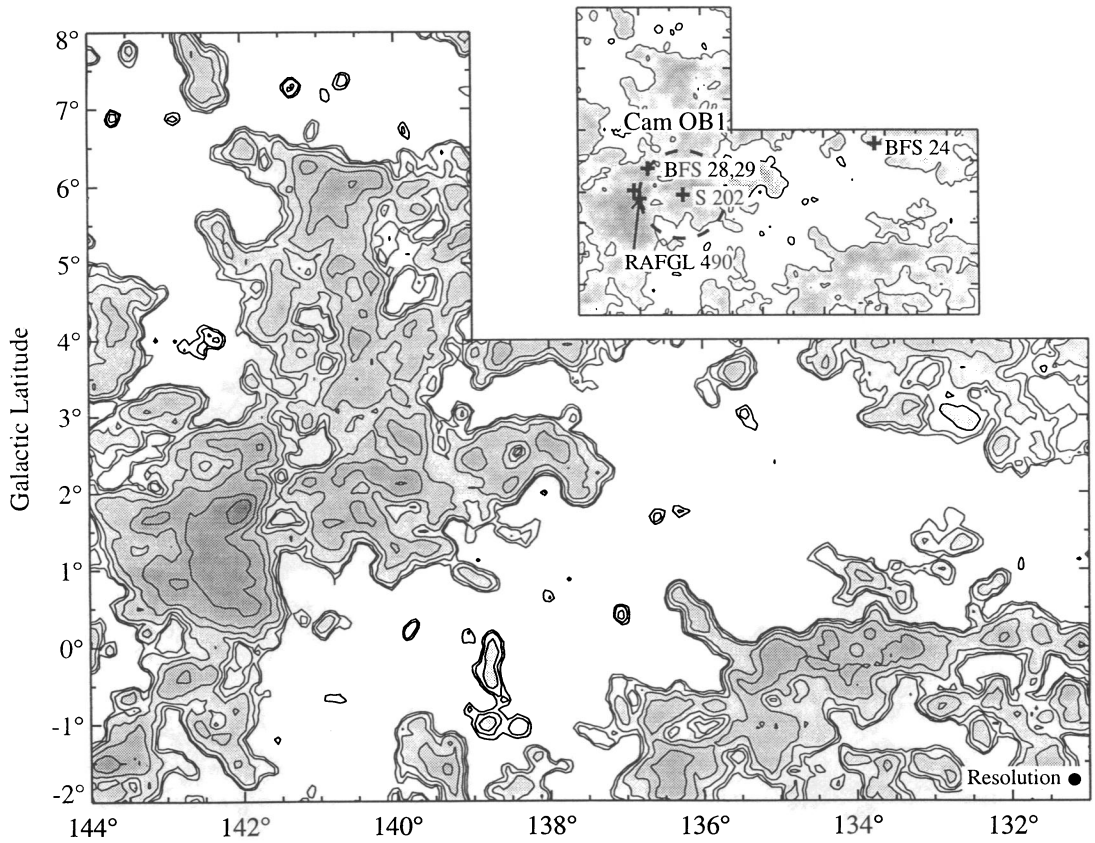

FIG. 4*a*

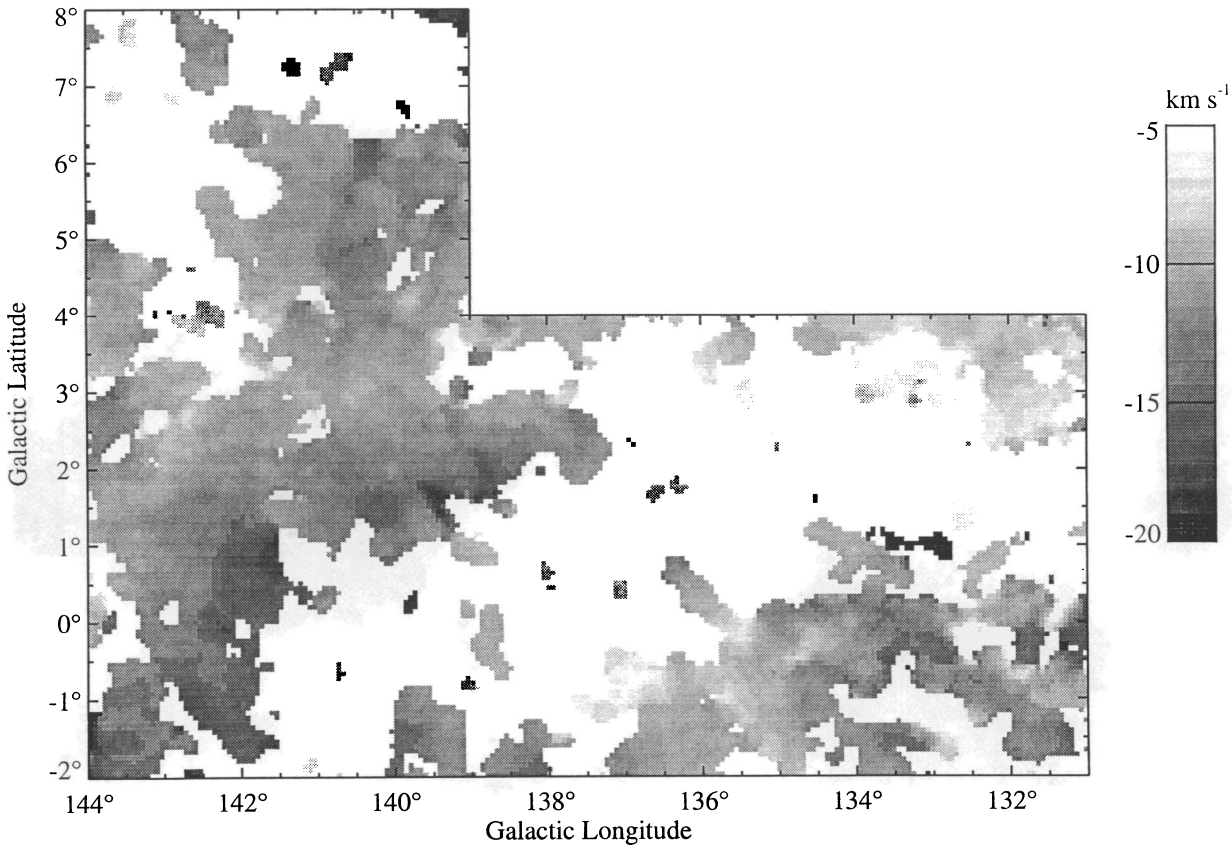

FIG. 4*b*

FIG. 4.—(*a*) Spatial map of the CO emission in Cam OB1, integrated over the range $-25 \leq V_{LSR} \leq -5$ km s^{-1}. Contours are 0.5, 1, 2, ... K km s^{-1}. The locations of the star-forming regions discussed in the text are indicated in the inset, which is drawn with only the lowest contour level. The dashed line shows the angular size of S202. The cloud complex associated with Cam OB1 is labeled. (*b*) Emission-weighted mean velocity of the CO emission for the same velocity range. The gray-scale representation of velocity covers $-20 \leq V_{LSR} \leq -5$ km s^{-1}.

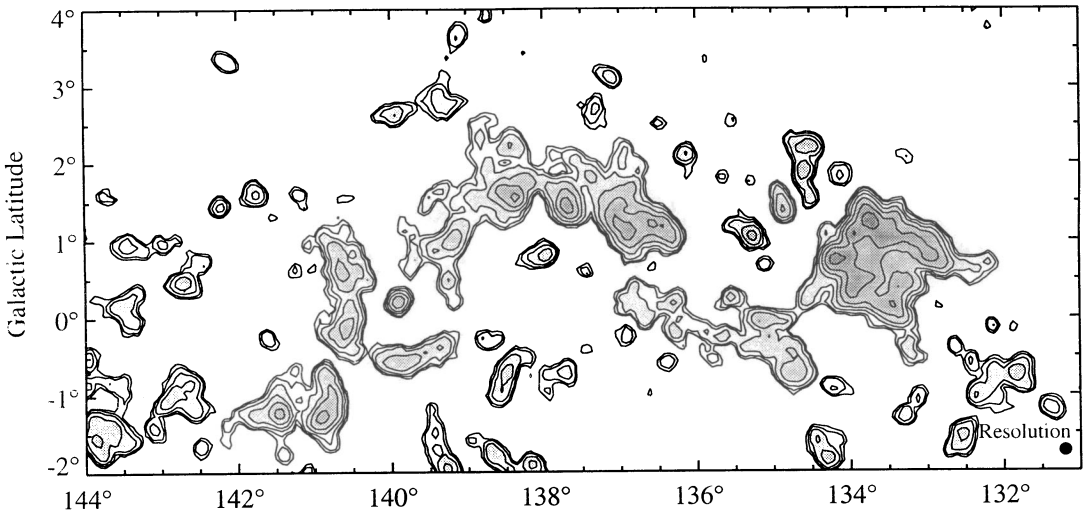

FIG. 5a

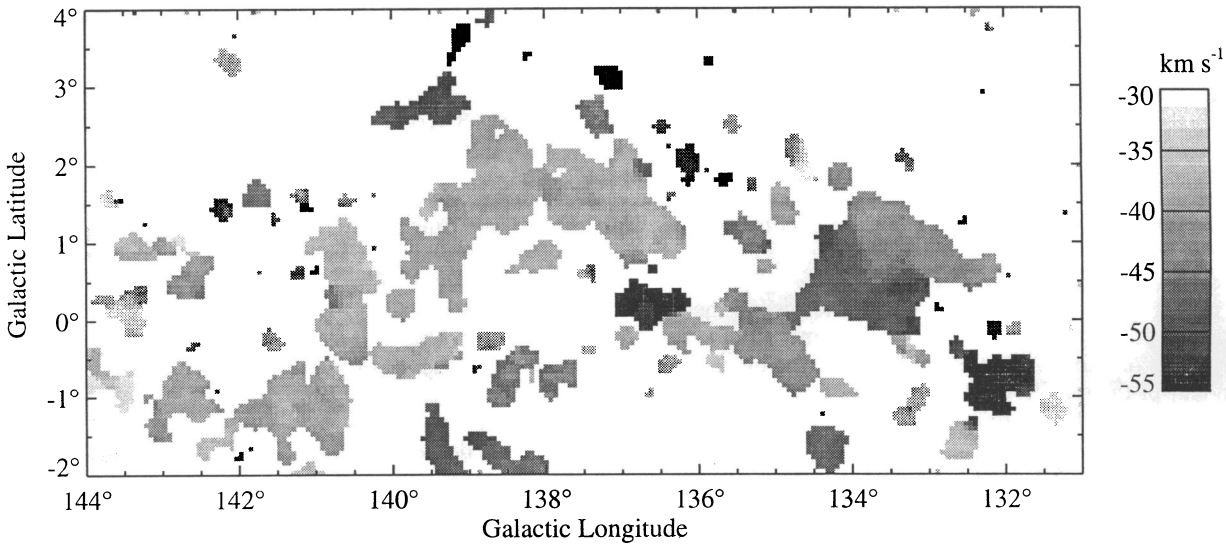

FIG. 5b

FIG. 5.—(*a*) CO emission in the Perseus arm, integrated over the range $-60 \leq V_{LSR} \leq -25$ km s^{-1}. Contours are 0.5, 1, 2, ... K km s^{-1}. (*b*) Emission-weighted mean velocity of the CO emission for the same velocity range. The gray-scale representation of velocity covers $-60 \leq V_{LSR} \leq -25$ km s^{-1}.

the Galactic equator, demonstrating that the wide latitude coverage here is indispensable for detecting clouds at the edge of the Galaxy: merely following the distant warped plane is inadequate. Interestingly, most of the distant clouds in our survey are displaced toward positive latitudes, but the most distant of all, cloud 2 of Digel et al. (1994), is 1° below the equator. All the distant clouds in Figure 7 lie below longitude $l = 138°$. This is probably because the kinematic Galactocentric distance corresponding to $V_{LSR} = -60$ km s^{-1}, the nearer velocity limit of the map, increases rather steeply with longitude (Fig. 1*a*).

3.2. *Clouds in the Perseus Arm*

Many of the Perseus arm molecular clouds are well defined and separated from others in position and radial velocity and possess distinct edges; moreover, because all have roughly the same distance, properties such as size and mass can be calculated fairly unambiguously. Local and Cam OB1 clouds are much less easy to characterize, owing largely to their uncertain distances; it is evident also from a glance at Figures 3*a* and 4*a* that partitioning the emission there into clouds is no easy matter. Local and Cam OB1 clouds will not be considered further here; the reader is referred to Lyder (1996).

Clouds in the Perseus arm were identified from the spatial map of Figure 5, and in *l*, *v* and *b*, *v* projections. The actual spatial and velocity boundaries of the clouds were determined using ordinary integrated maps, not the moment analysis-derived maps used to make the figures. The largest complexes can generally be partitioned into a few component clouds, but in some instances spatial or velocity blending is too severe to allow that to be done. Only clouds with well-defined, single-peaked spatial maps and composite spectra are listed in Table 3; all were independently identified by two of the authors (D. A. L. and S. W. D.). The clouds in Table 3 constitute ~43% of the total CO intensity in the velocity range of the Perseus arm.

For simplicity, we adopt a uniform distance D = 2.5 kpc for the molecular clouds in the Perseus arm. This is considerably less than the typical kinematic distances of ~4 kpc (on the assumption of a flat rotation curve with $R_\odot = 8.5$ kpc and $V_\odot = 220$ km s^{-1}), but streaming motions of amplitude ~15–20 km s^{-1} have long been known for the Perseus arm in

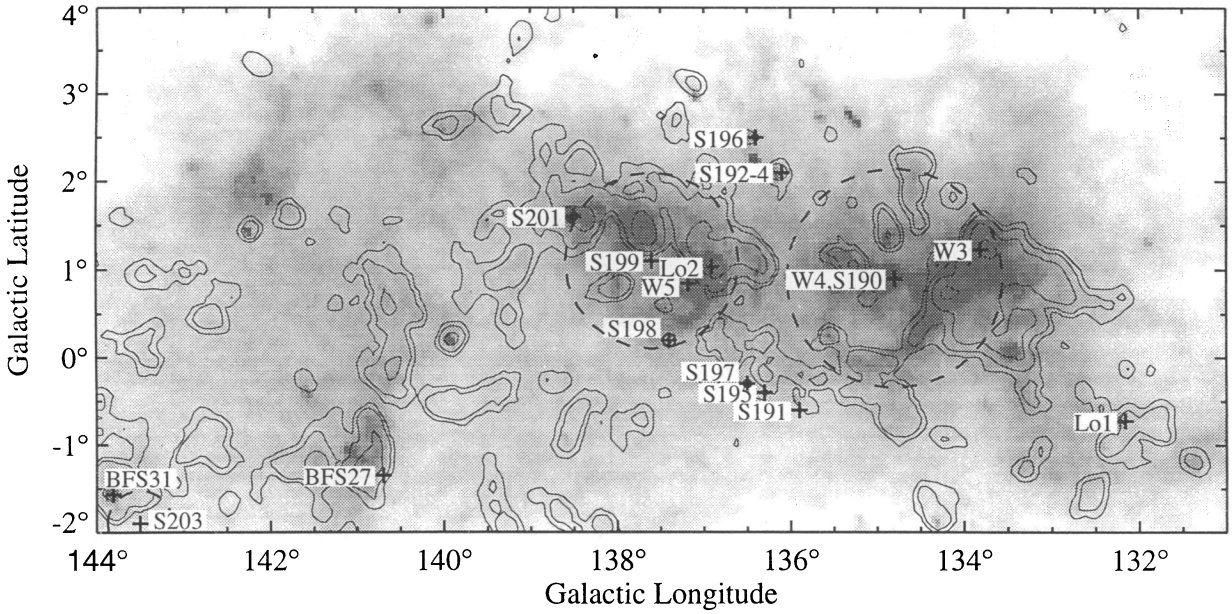

FIG. 6.—Radio and optical H II regions in the Perseus arm against a gray-scale representation of the *IRAS* 60 μm intensity (*IRAS* Explanatory Supplement, 1988). Every other contour from Fig. 4 is overlain to locate the CO emission in the Perseus arm. Sharpless (1959) H II regions in the Perseus arm are indicated along with their angular sizes (*dashed lines*). BFS 27 and BFS 31 are optical H II regions observed in CO by Blitz et al. (1982), and Lo 1(132°.157, −0°.725) and Lo 2(136°.913, 1°.033) are H II regions observed in radio recombination lines of hydrogen by Lockman (1989).

the outer second quadrant (e.g., Humphreys 1976; see also Brand & Blitz 1993). A distance of 2.5 kpc is consistent with optical determinations of the distances of S190 and S199 (Brand & Blitz 1993; see also Fig. 6).

The radius r of a cloud is defined in terms of the area subtended by the contour at half-maximum integrated intensity. This definition has the advantage of being relatively independent of the sensitivity of the survey and may be easily corrected for the finite resolution of the telescope, $r = D[A/\pi - (\Delta\theta/2)^2]^{1/2}$, where A is the solid angle of the half-peak intensity contour and $\Delta\theta$ is the FWHM of the telescope's main beam.

For each cloud, the FWHM velocity width Δv was determined by fitting a Gaussian to the composite spectrum derived by summing all of the spectra within the l and b range that define the cloud. The total intensity I_{CO} (K km s^{-1} deg^2) and luminosity in the CO line $L_{CO} = I_{CO} D^2$ are derived from the Gaussian profile.

Cloud masses have been estimated in two standard ways: from the integrated CO 1–0 line intensity, and from the derived radii and line widths via the assumption of virial equilbrium. The mass derived from the CO intensity is given by

$$M_{CO} = 6.2(X/1.9)L_{CO}\, M_\odot\,, \qquad (1)$$

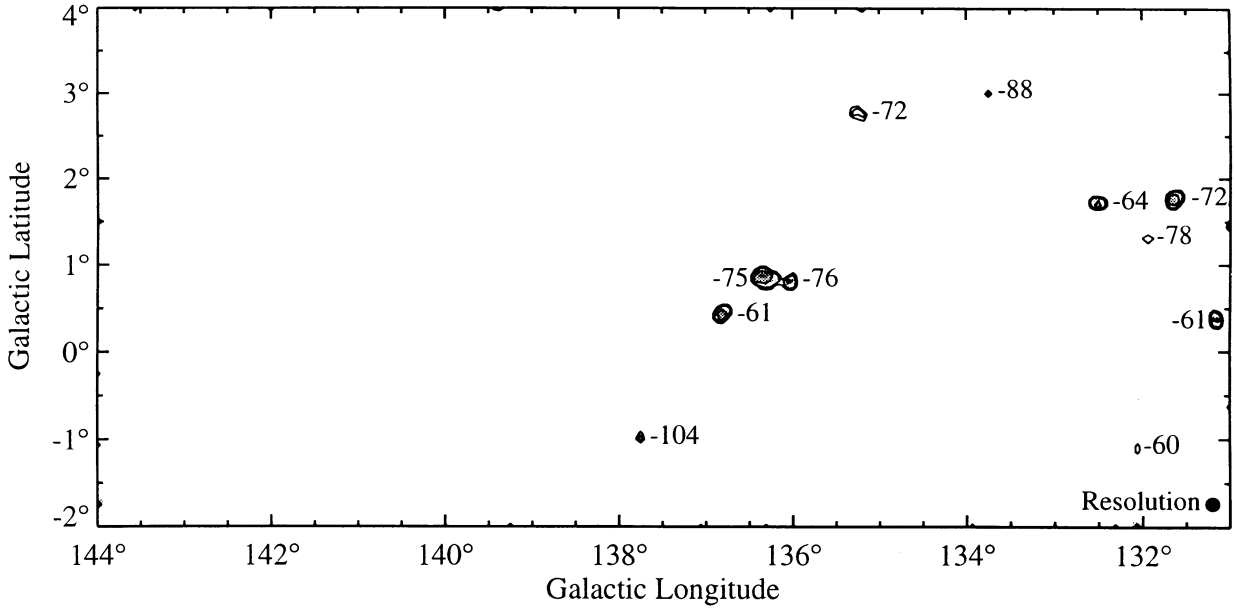

FIG. 7.—Integrated CO emission in the outer arm and far outer Galaxy ($-130 \le V_{LSR} \le -60$ km s^{-1}), calculated using the method described in the text. The contour levels are 0.25, 0.5, 1.0, ... K km s^{-1}, the lowest being approximately 3 σ for all the clouds shown. The clouds are labeled with their emission-weighted mean velocities in km s^{-1}.

TABLE 3

PARAMETERS OF PERSEUS ARM CLOUDS

Number	l	b	V_{LSR}[a] (km s^{-1})	Δv[b] (km s^{-1})	r[c] (pc)	L_{CO}[d] (10^3 K km s^{-1} pc^2)	M_{CO}[e] (10^3 $M_\odot$)	M_{vir}[f] (10^3 $M_\odot$)
1	131°.3	−1°.2	−34.5	1.9	4.7	0.49	2.0	4.1
2	131.8	−0.7	−53.9	3.8	3.6	0.92	3.9	12
3	132.2	−1.0	−55.2	2.5	7.1	0.85	3.6	11
4	132.2	0.7	−41.8	3.6	4.5	0.85	3.6	14
5	132.5	−1.5	−37.7	2.7	3.6	0.84	3.5	6.5
6	132.6	−0.4	−50.7	2.8	2.8	0.17	0.7	5.2
7	133.0	0.9	−43.0	3.9	9.3	6.22	26	34
8	133.2	2.1	−41.9	4.2	18	0.19	0.8	77
9	133.3	−1.3	−39.0	2.6	2.8	0.37	1.5	4.6
10	133.7	1.2	−40.9	5.9	4.5	7.97	33	38
11	133.9	0.4	−47.6	5.8	9.4	7.84	33	78
12	134.1	0.8	−48.4	4.9	5.4	7.04	29	31
13	134.1	1.8	−43.0	1.8	2.4	0.37	1.5	1.9
14	134.3	−1.8	−48.8	3.4	4.5	0.73	3.1	13
15	134.5	0.3	−47.3	3.4	6.6	0.61	2.6	18
16	134.5	2.2	−30.7	2.3	2.4	0.73	3.1	3.1
17	134.6	1.9	−30.0	3.0	3.9	0.49	2.0	8.5
18	134.6	1.9	−36.9	2.6	1.8	0.31	1.3	3.0
19	134.7	−0.7	−42.7	3.8	7.1	1.82	7.6	24
20	134.7	2.2	−40.8	2.5	5.2	0.34	1.4	7.8
21	134.8	0.0	−46.3	3.7	3.9	0.41	1.7	13
22	134.9	1.5	−39.9	4.6	3.6	1.14	4.8	18
23	135.0	0.0	−36.3	3.0	4.2	0.45	1.9	9.3
24	135.1	0.0	−44.8	3.5	3.9	0.88	3.7	12
25	135.3	1.1	−45.0	4.6	2.4	1.23	5.2	12
26	135.5	0.3	−43.4	2.4	3.2	0.31	1.3	4.3
27	135.6	0.2	−36.2	2.5	3.9	0.19	0.8	6.0
28	136.1	2.1	−46.3	3.3	2.8	0.40	1.7	7.3
29	136.4	0.2	−56.4	3.6	4.5	0.67	2.8	14
30	136.5	1.2	−36.4	3.7	7.6	4.40	18	25
31	136.7	1.9	−49.9	2.1	1.8	0.24	1.0	1.9
32	136.9	1.1	−40.6	3.6	3.9	2.07	8.7	12
33	137.0	1.3	−38.5	6.2	5.4	9.19	38	50
34	137.2	3.1	−50.7	2.0	2.4	0.35	1.5	2.3
35	137.3	2.7	−45.5	2.9	2.8	0.35	1.4	5.5
36	137.7	1.5	−38.9	3.8	4.2	3.86	16	14
37	137.8	−0.7	−45.0	2.7	5.4	0.53	2.2	9.5
38	138.0	0.8	−38.4	3.0	4.5	0.91	3.8	9.8
39	138.5	−0.8	−45.6	2.8	6.8	1.46	6.1	13
40	138.5	−0.7	−37.4	4.4	1.8	0.24	1.0	8.4
41	138.5	1.6	−38.7	2.8	4.5	4.84	20	8.8
42	138.5	2.2	−39.6	2.6	5.4	0.82	3.4	8.8
43	139.0	1.6	−39.1	2.0	4.5	0.61	2.6	4.4
44	139.2	0.4	−39.9	2.0	2.4	0.45	1.9	2.4
45	139.2	1.0	−39.6	2.7	7.6	1.71	7.1	13
46	139.4	−0.4	−37.2	4.6	4.7	0.85	3.6	24
47	139.9	−0.5	−39.0	4.2	6.6	1.83	7.7	28
48	139.9	0.2	−40.0	3.2	1.0	1.06	4.4	2.4
49	139.9	2.6	−50.2	3.0	3.9	0.73	3.1	8.5
50	140.6	−0.1	−39.2	4.1	5.6	3.22	14	23
51	140.6	0.7	−37.9	3.6	6.4	4.06	17	21
52	140.9	−1.1	−40.4	4.1	6.8	5.61	24	28
53	141.5	−1.2	−40.8	2.7	3.9	3.31	14	6.9
54	141.8	1.6	−47.0	2.9	3.2	0.54	2.2	6.3
55	142.2	1.4	−45.7	3.0	2.4	0.35	1.5	5.1
56	142.6	0.5	−44.2	3.9	3.2	1.06	4.4	12
57	143.4	0.9	−39.3	2.8	5.6	0.61	2.6	11
58	143.6	0.2	−34.3	2.9	5.4	0.53	2.2	11
59	143.8	−1.5	−32.2	2.6	5.8	1.98	8.3	9.4
Totals							429	877

[a] Line-of-sight velocity with respect to the local standard of rest, from a Gaussian fit to the cloud's composite spectrum.

[b] FWHM of the Gaussian fit.

[c] Cloud radius at the half-maximum contour of W_{CO}, corrected for the size of the beam.

[d] CO luminosity, integrated from the fit to the cloud's composite spectrum.

[e] Cloud mass derived from L_{CO} on the assumption that $X = 1.9 \times 10^{20}$ cm^{-2} (K km s^{-1})$^{-1}$ with an additional factor of 1.36 for helium.

[f] Mass of a uniform, spherical cloud in virial equilibrium $M_{vir} = 5/(8\ G \ln 2)\ (4/3)^{1/2}\ r\ \Delta v^2$, where the factor $(4/3)^{1/2}$ corrects the half-maximum radius r to the full radius of a uniform, spherical cloud.

including a factor of 1.36 for helium and heavier elements (Allen 1973), where X is the assumed constant ratio of H_2 column density to integrated CO line intensity in units of 10^{20} cm^{-2} (K km s^{-1})$^{-1}$ and L_{CO} is in K km s^{-1} pc^2. We use the standard X-ratio of Strong et al. (1988), 1.9×10^{20} cm^{-2} (K km s^{-1})$^{-1}$ after scaling as indicated in § 2. The virial mass, M_{vir}, of a molecular cloud of half-peak intensity radius r (pc) and FWHM velocity width Δv (km s^{-1}) is defined as the mass of an isolated, isothermal, nonrotating, spherical cloud with the same size and velocity dispersion in gravitational virial equilibrium. Magnetic forces are assumed negligible. For a cloud with uniform density, the virial mass is (e.g., Digel et al. 1994)

$$M_{vir} = 242.5 r \Delta v^2 \, M_\odot , \qquad (2)$$

where r is in pc and Δv is in km s^{-1}, and a factor of $(4/3)^{1/2}$ is included to correct the half-maximum radius to the full radius of a uniform, spherical cloud. The derived quantities are tabulated in Table 3.

The CO luminosity, L_{CO}, and line widths, Δv, of molecular clouds are somewhat better defined observationally than their radii and can be used to compare the $N(H_2)/W_{CO}$ ratio (or X ratio) for populations of clouds. Figure 8 shows the relation between CO luminosity and line width for the clouds in Table 3. The fit is derived as the bisector of least-squares fits of L_{CO} versus Δv and of Δv versus L_{CO}; error bars are not shown because the intrinsic scatter is much greater than the uncertainties in the luminosities or line widths. The dashed line in the figure is the mean luminosity–line width relation found for the largest molecular complexes in the inner Galaxy ($R \sim 3$–8 kpc) by Dame et al. (1986). The luminosity-weighted mean offset of the clouds in Figure 8 from the luminosity–line width relation of Dame et al. (1986) corresponds to a factor of 5 ± 2, i.e., for a given velocity width, clouds in the Perseus arm are 5 ± 2 times fainter in CO. The mass-weighted average ratio of the virial and CO masses of the clouds in Table 3 is 2 ± 1. These factors are in acceptably good agreement, considering the large cloud-to-cloud scatter. We adopt 3.5 ± 2 as the factor of increase in X in the Perseus arm relative to the inner Galaxy; the luminosity–line width determination is given more weight because the virial masses are relatively uncertain. Similar increases in X were found for molecular clouds in the outer Galaxy by Mead & Kutner (1988), Digel, Bally, & Thaddeus (1990), Sodroski (1991), and Ungerechts, Umbanhowar, & Thaddeus (1996), all of whom also compared luminosity–line width relations or virial masses and CO-inferred masses. An increase in the X ratio from the molecular ring to the Perseus arm may result from known or expected metallicity or temperature gradients (e.g., Digel et al. 1990).

The mass distribution of the clouds in Table 3 is shown in Figure 9, along with the best-fitting power law. The power-law index α for a cumulative mass distribution $N(>M) = AM^{-\alpha}$ is 0.88 ± 0.14, derived using the maximum likelihood method of Crawford, Jauncey, & Murdoch (1970) for a completeness limit of $2 \times 10^3 \, M_\odot$ and a maximum possible cloud mass large enough for the asymptotic solution in Crawford et al. (1970) to apply. The value of α found here is somewhat larger than reported by others (Table 4) but still consistent with the previous claims that most of the molecular mass is contained in the largest complexes, i.e., $\alpha < 1$. Because the definition here of clouds is somewhat subjective, we investigate in the Appendix the mass spectrum inferred from two alternative methods of cloud definition, as well as the effect of limited linear resolution. There it is shown that the index α is fairly robust, not strongly dependent on the algorithms used to identify the clouds, or even on the resolution of the data. From these less

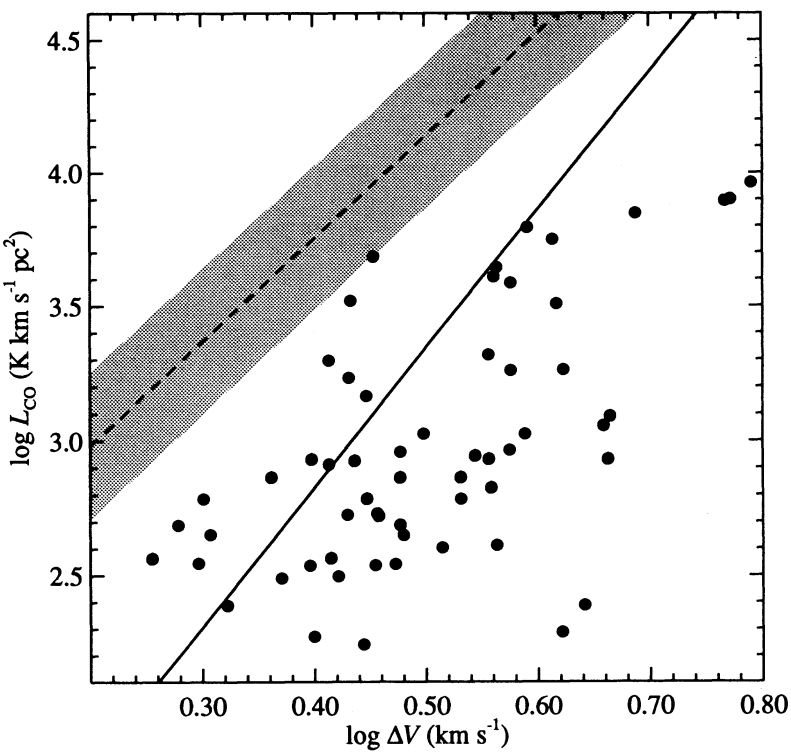

FIG. 8.—Luminosity–line width scatter diagram for the clouds in the Perseus arm (Table 3). The dashed line, log $L_{CO} = 2.30 + 3.16 \log \Delta V$, is the luminosity–line width relation derived by Dame et al. (1986) for the largest complexes of molecular clouds in the inner Galaxy, translated to $R_\odot = 8.5$ kpc and the current intensity scale for CO. The shaded area indicates the approximate 1 σ dispersion of the Dame et al. (1986) clouds about the fit. The solid line, log $L_{CO} = 0.84 + 4.25 \log \Delta v$, is a fit (mean of the bisectors) to the clouds observed here in the Perseus arm.

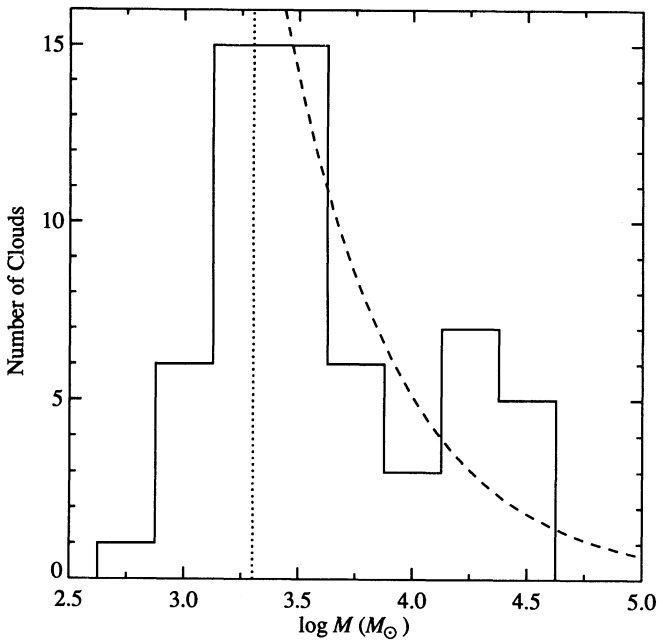

FIG. 9.—Distribution of CO luminosity-inferred masses of molecular clouds identified by the manual method in the Perseus arm (Table 3) with the best-fitting power law, $N(M) \propto M^{-0.88}$ for $M > 2 \times 10^3\ M_\odot$ shown. The adopted completeness limit is indicated by the dotted line.

subjective analyses, we derive $\alpha = 0.65 \pm 0.15$. Massive clouds, e.g., those associated with W3 (Fig. 6), partially blended and difficult to partition with well-defined composite spectra, were certainly missed in constructing Table 3, and such omission tends to steepen the spectrum. Automatic methods of identification include these blended, massive clouds that would not be selected by hand. Because they are not uniformly distributed in mass, blended and otherwise poorly defined clouds are important for estimation of the mass spectrum, even if their masses are only approximately known.

3.3. *Surface Density and Arm-Interarm Contrast of Molecular Gas*

The kinematic separation of the Perseus and local molecular clouds in Figure 1 may be influenced by streaming motion but cannot be caused by it entirely: there is a wealth of evidence that the interarm gap is real. Although large-scale deviations from uniform circular motions caused by streaming in the Perseus arm are well known in this region, optical observations as mentioned have long provided evidence for a large region almost free of H II regions, OB stars, and other Population I members that corresponds qualitatively to the kinematic gap found here (e.g., Morgan, Sharpless, & Osterbrock 1952). The streaming motions constitute a *perturbation*, which may alter the apparent width of the gap but not create it. Kimeswenger & Weinberger (1989) summarize the optically derived information on Galactic structure in the second quadrant and find an interarm gap of ~ 1 kpc between the local and Perseus arms over the longitude range of the W3 region.

With precise knowledge of the velocity field in the outer Galaxy, the noncircular motions could be taken into account explicitly and the distribution of the surface density of molecular gas could be determined. Brand & Blitz (1993) have attempted to derive the velocity field in the outer Galaxy from CO observations of H II regions with optically determined distances. Owing to the large area and the relatively few H II regions suitable for study, the velocity field of Brand & Blitz (1993) is too crudely defined for the present purpose. In particular, only three H II regions, only two of which lie in the Perseus arm, were used to define the velocity field in the longitude range of interest here, $l = 131°$–$144°$. Even if the velocity field is perfectly known, the internal and cloud-to-cloud velocity dispersions of the molecular gas limit the resolution with which the surface density may be determined.

Derivation of the distribution of molecular gas with R and z in the outer Galaxy first requires transforming the observed distribution of main-beam temperature $T_{\rm mb}(l, b, v_{\rm LSR})$ into the corresponding gas volume density distribution $\rho(R, z)$, where z is the vertical displacement from the Galactic plane. Expressed in convenient units, the volume density is given by (Grabelsky et al. 1987; Digel 1991)

$$\rho = 6.1 \times 10^{-3}(X/1.9)T_{\rm mb}\,|\,dV_{\rm LSR}/dD\,|\,M_\odot\ {\rm pc}^{-3}\ , \qquad (3)$$

where X again is in units of 10^{20} cm^{-2} (K km s^{-1})$^{-1}$, $T_{\rm mb}$ is in K, and the velocity gradient is in km s^{-1} kpc^{-1}, again on the assumption that the mean atomic weight per H atom $\mu = 1.36$ (Allen 1973). The value of μ changes only slowly with R, because the gradient of the logarithm of the helium abundance is only about -0.02 kpc^{-1} at the solar circle (Güsten & Mezger 1982), and heavier metals contribute little to μ; here it is assumed independent of R. For consistency with previous work, and because the gradient of X is still poorly known, the commonly adopted $X = 1.9 \times 10^{20}$ cm^{-2} (K km s^{-1})$^{-1}$ (Strong et al. 1988), scaled as in § 2, is assumed for all Galactocentric distances in the results presented below.

Surface density profiles for different longitude ranges, derived from integration of $\rho(R, z)$ over z, are shown in Figure 10. The CO data for $b = -2°$ to $+4°$ were used to derive ρ. The concentrations of molecular gas in the local and Perseus arms stand out, and as one might expect there is more fluctuation with l in the local emission owing to the much smaller linear dimensions sampled. The resolution in R of the profiles is ~ 1 kpc owing to the several km s^{-1} random component of cloud velocities.

The observed contrast in surface density of molecular gas between the Perseus arm and the interarm region (i.e., the ratio of the peak surface density in the Perseus arm to the 3 σ upper limit of the interarm regions), is at least 25, and even greater for

TABLE 4

COMPARISON WITH OTHER DETERMINATIONS OF THE MASS SPECTRUM OF MOLECULAR CLOUDS

Study	Region	Mass Range ($10^3\ M_\odot$)	Spectral Index α
Dame 1983	Perseus arm, $l = 104°$–$128°$	1–600	0.45 ± 0.08
Casoli et al. 1984	Perseus arm, $l = 108°$–$112°$	0.2–200	0.5 ± 0.1
Sanders, Scoville, & Solomon 1985	Inner Galaxy, $l = 10°$–$90°$	20–2000	0.58
Solomon et al. 1987	Inner Galaxy, $l = 8°$–$90°$	2–5000	0.50 ± 0.12
Present work (manual)	Perseus arm, $l = 131°$–$144°$	2–40	0.88 ± 0.14
Present work (box)	Perseus arm, $l = 131°$–$144°$	2–200	0.65 ± 0.15

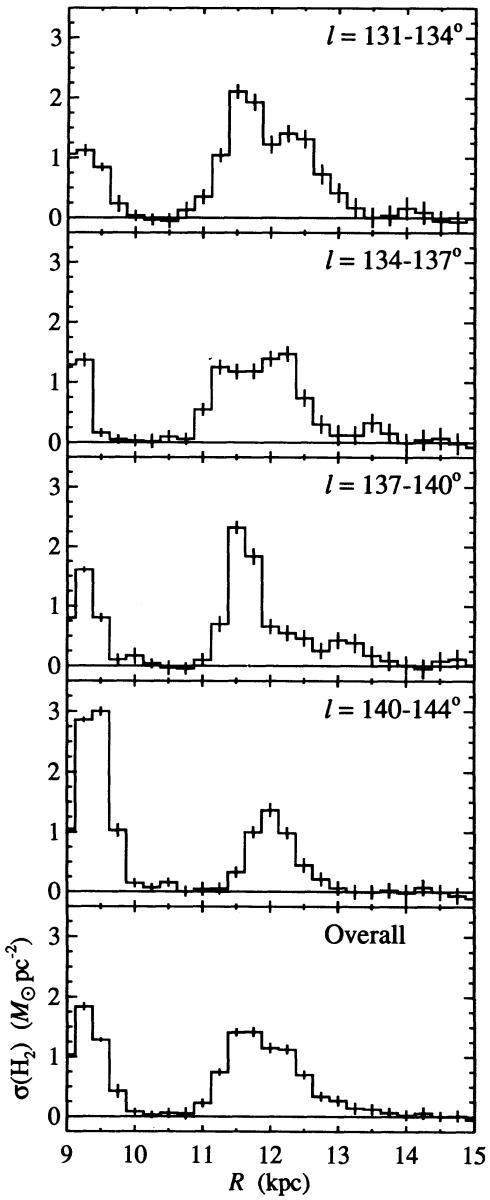

FIG. 10.—Radial surface density profiles for the indicated longitude ranges, with 0.25 kpc bins in R. The local emission lies near kinematic Galactocentric radius ~9 kpc, and the emission in the Perseus arm lies at ~11–13 kpc. Error bars correspond to 3 σ for each bin.

some of the longitude ranges. This is consistent with the ratio that may be estimated roughly from the composite spectrum in Figure 2, where the peak intensity in the Perseus arm is ~20 times greater than the average level at interarm velocities. A large arm-interarm contrast is evident on each of the longitude ranges shown in Figure 10, which indicates that the high contrast we find is very unlikely to result from fluctuations of the distribution of molecular clouds along the local and Perseus arms. The few clouds kinematically within the interarm gap (Fig. 1) represent very low surface densities in Figure 10. Follow-up observations in multiple transitions of CO could determine whether these clouds represent "cold" clouds as defined by Solomon, Sanders, & Rivolo (1985). Luminosity–line width studies might also help if the distances of the clouds could be determined.

This 25:1 arm-interarm contrast in molecular gas is among the largest yet determined from studies of the Milky Way and external galaxies. Typical findings for external galaxies M31 and M51 are 3–5:1 averaged along arms (e.g., Lo et al. 1987; Vogel, Kulkarni, & Scoville 1988; Adler et al. 1992). Peak contrasts of 20:1 or more have been found for small areas (e.g., Stark 1985 in M31; Adler et al. 1992 in M51), but that is probably the result of the clumpiness of molecular gas on small scales. The surface density of molecular gas is evidently somewhat greater than average in the region of our survey, but we estimate from the survey of Dame et al. (1987) that it is enhanced by less than 25% over the average along the entire arm. Arm-interarm contrasts similar to those in the W3 region were found in the recent study by Ungerechts et al. (1996) of the section of the Perseus arm in the longitude range $l = 107°$–$116°$. The lower limit on the arm-interarm contrast found here is about twice as great as the contrast reported by Grabelsky et al. (1987) from the longitude profile of CO intensity across the tangent direction of the Carina arm.

The recent work of Carey (1995) suggests that the X ratio is greater in the interarm region between the Perseus and outer arms than in the outer arms and serves as a caveat to interpretation of arm-interarm contrasts. Carey's findings are based on comparisons of virial masses and CO luminosities of 35 molecular clouds resolved in a sensitive small-area survey. The magnitude of the difference in X ratio is very uncertain but could be as much as a factor of a few. If X is enhanced in interarm regions in general, then the arm-interarm contrast derived above would be decreased, as it would be for all studies cited, because the surface density profiles, calculated for a constant X ratio, are essentially scaled profiles of CO surface emissivity.

The possibility that significant amounts of cold molecular gas exist in the interarm gap can probably be ruled out. A recent study of CO and HCO^+ absorption along lines of sight in the outer Galaxy has found no absorption at interarm velocities (de Geus 1995). The model of Tilanus & Allen (1989) for the arm and interarm gas in M51 and M83 indicates a very low surface density contrast in molecular gas; the gas in the arms is just warmer and aggregated into larger associations than the interarm gas. This seems to be counter to what we observe for the Perseus arm. One reason may be that the Perseus arm may be close to the corotation radius of the Milky Way, with the result that streaming through the arm might not proceed at a great rate and molecular gas may tend to accumulate in the arm.

3.4. *Comparison with the Distribution of WB Sources*

Wouterloot et al. (1990; hereafter WBBK) studied the distribution of molecular gas in the outer Galaxy under the assumption that the molecular gas is proportionately traced by massive star-forming regions embedded in molecular clouds. Wouterloot & Brand (1989, hereafter WB) obtained CO spectra toward more than 1000 *IRAS* point sources (*IRAS* Explanatory Supplement 1988) in the outer Galaxy with infrared fluxes and colors characteristic of massive star-forming regions. WBBK used the radial velocities of CO lines detected toward the point sources to determine kinematic distances. Selecting the subset of the sources that would be detectable at even the greatest Galactocentric distances of sources detected, approximately equivalent to requiring a far-infrared luminosity $\geq 2000\ L_\odot$, WBBK determined the distribution of massive star-forming regions across the outer Galaxy.

On the longitude and latitude range of the W3 region, 56

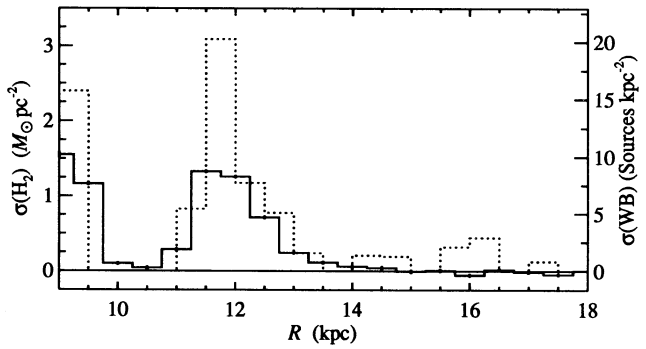

FIG. 11.—*Solid line*: surface density vs. Galactocentric distance for molecular gas, calculated for the entire survey range, $l = 131°$–$144°$ with 0.5 kpc bins in R. The statistical uncertainties in the surface density are quite small at this resolution; 3 σ error bars are indicated. *Dotted line*: Surface density profile of WB sources, referred to the scale on the right, above the completeness limit in the same longitude and latitude range. The profile is calculated for a bin size of 0.5 kpc that is offset by 0.25 kpc from the molecular gas profile for clarity.

sources were detected by WB, 28 with fluxes greater than the completeness limit. Figure 11 shows the profile of the surface density of these sources, corrected for the areas of the plane sampled in each Galactocentric distance range and for the limited sampling range in z, using the scale heights derived by WBBK. For comparison, the profile of the surface density of molecular gas, calculated with the same grid size, is also shown. The profiles are generally similar, with a rough proportionality of one luminous WB source per $10^5\ M_\odot$ of molecular gas (using the standard X ratio). But significant differences are also apparent. The surface density of WB sources seems to be enhanced in the regions with greatest molecular surface density, suggesting that the star formation efficiency depends on surface density. This is not likely to be an effect caused by different velocity dispersions for the molecular clouds and the WB sources; the WB sources are likely to have even greater velocity dispersions than the clouds, which would tend to smear out their distribution in (kinematic) Galactocentric distance. The distribution of WB sources appears to have a peak near $R = 16$ kpc, the approximate Galactocentric distance of the outer arm in the W3 region (e.g., Henderson et al. 1982). The peak in WB sources does not have a counterpart in molecular gas. This suggests either a greatly increased star formation efficiency in the outer arm or that the X ratio appropriate for the outer arm, essentially undetected in CO here, is much greater than the standard value.

The correspondence of the distributions of molecular gas inferred from a CO survey and from WB sources has also been investigated for the longitude range $l = 107°$–$116°$ (Digel 1991) using the CO survey of Ungerechts et al. (1996), with similar findings about the apparently nonlinear variation of the surface density of WB sources in regions of greatest surface density. On $l = 107°$–$116°$, the outer arm is much closer, near $R = 13$ kpc, and it is not strongly detected in WB sources.

4. CONCLUSIONS

The outer Galaxy toward the well-known H II regions W3, W4, and W5 contains a rich and intricate tangle of molecular gas, both locally in the Cam OB1 region and in the Perseus arm, much of which was previously undetected. The local foreground gas is particularly extensive, covering about $\frac{2}{3}$ of the 98 deg^2 surveyed and apparently segmented into bands $\sim$200 pc and $\sim$800 pc distant. The $\sim$1–2 kpc kinematic gap between the local and Perseus arms is remarkably free of molecular clouds. The large molecular clouds in the Perseus arm associated with W3, W4, and W5 and a number of Sharpless H II regions are connected by extensive filamentary molecular gas which fell below the sensitivity or beyond the range of previous studies of the region; the idealization of molecular clouds as high-density condensations of the interstellar gas with sharp boundaries and well-defined masses clearly requires qualification in this part of the Perseus arm. Little molecular gas has been found at greater Galactocenric distances. A notable exception is a cloud at a kinematic distance of 28 kpc from the Galactic center previously detected in a deep, selective survey of H I emission peaks near the edge of the Galaxy (Digel et al. 1994).

The molecular clouds in the Perseus arm are found to be somewhat underluminous in CO for a given velocity width than the largest clouds in the inner Galaxy, and their virial masses are somewhat greater than their luminosity-inferred masses for the standard $N(H_2)/W_{CO}$ ratio X. These deficiencies suggest an increase of X by a factor 3.5 ± 2 relative to the value that applies to the giant molecular clouds in the inner Galaxy, an increase consistent with what some other studies have indicated for the Galactocentric distance range $R \sim 11$–13 kpc.

The cumulative mass spectrum of the molecular clouds observed in the Perseus arm has been determined in several ways from the survey and appears to be described adequately by a power law with index 0.65 ± 0.15. This spectrum is somewhat steeper than that derived by others elsewhere in the Perseus arm and in the inner Galaxy. The mass spectrum can be determined only to the extent that individual clouds can be identified, and at the high-mass end, this identification is complicated by the blending of clouds. An automatic method was applied to divide blended emission into clouds objectively; the spectral index was found to be remarkably independent of the intensity threshold used.

The surface density of molecular gas in the outer Galaxy shows the expected concentration of gas in the Perseus and local arms and a very clear interarm gap with contrast at least 25:1 on the assumption of a constant X ratio. This is about the largest arm-interarm contrast yet found from studies of the Milky Way and external galaxies. Streaming motions, which can be taken into account only very approximately, may perturb the location of the gap, but they do not modify the surface density contrast.

The distribution of molecular gas in the part of the outer Galaxy covered by the survey is approximately traced by the distribution of luminous star-forming regions cataloged by Wouterloot & Brand (1989), with a proportionality of about one source with infrared luminosity $\geq 2000\ L_\odot$ per $10^5\ M_\odot$ of molecular gas. The primary difference is that the surface density of star-forming regions appears to be more peaked than that of the molecular gas, suggesting that the star formation efficiency depends nonlinearly on the surface density of molecular gas. The relatively large number of Wouterloot & Brand (1989) sources seen near $R = 16$ kpc is evidence for a strong increase in the star formation efficiency or the X ratio there.

We thank T. M. Dame and E. S. Palmer for maintaining the CfA 1.2 m telescope and the many improvements in reliability and sensitivity from which this work has benefited.

APPENDIX

MASS SPECTRUM OF MOLECULAR CLOUDS

The crucial difficulty in determining the mass spectrum of molecular clouds is the question of cloud definition: how a cloud is carved out of the often intricate jumble of emission that is observed. Although some clouds are very well defined, others are severely blended in large complexes which are difficult to partition objectively. The loose use of terms such as cloud complexes, cloudlets, cloud cores, etc., is a measure of the ambiguity which afflicts this attempt. Owing to the subjective nature of cloud definition, the catalog in Table 3 is not necessarily complete, especially in regions in which blending complicates identification of individual clouds. Several algorithms for the objective, unbiased definition of clouds have been developed (e.g., Casoli, Combes, & Gerin 1984; Solomon et al. 1987; Williams, de Geus, & Blitz 1994). Unfortunately, even an objective method remains dependent on the resolution of the data to some degree. As discussed below, here we investigated automatic procedures to evaluate the sensitivity of the results to the method as well as to the angular resolution.

Two methods for automatic identification of clouds, one simple and one more sophisticated, were employed to evaluate the sensitivity of the spectral index to the method. The first uses surfaces of constant temperature in (l, b, V) space to define the boundaries of clouds. In this case a cloud consists of all adjacent pixels ($3'.75 \times 3'.75 \times 0.65$ km s^{-1}) with intensities greater than a given threshold intensity. This method is not completely satisfactory because it truncates the emission from the outer parts of the cloud, which in most cases is a large fraction of the total. The second method attempts to overcome this by using the ranges of l, b, and V for the pixels above the threshold in a cloud to define a box that surrounds the cloud. The luminosity of the cloud is determined by all the pixels within the box rather than just those above the intensity threshold. This method, although not perfect, seems to identify clouds of sizes and masses more consistent with what are found manually. It is essentially the same as that used by Solomon et al. (1987). Following Solomon et al. (1987), we extended the boxes by ± 2 km s^{-1} in velocity to further limit truncation of the velocity profiles of the clouds. However, unlike Solomon et al. (1987), we do not set a lower limit on the number of pixels a cloud must contain. The masses of the clouds defined by the box method are generally $\sim 50\%$ greater than those defined by the truncation method.

The mass spectrum of clouds in the W3 region was investigated for a wide range of threshold intensities using the truncation and box methods. The thresholds were chosen to be multiples (3, 5, 7, ...) of the 1 σ sensitivity of the survey (0.115 K rms per channel in the 10′ resolution data set). The spectral indices were derived using the maximum likelihood method of Crawford et al. (1970) and are not dependent on the binning of the distributions. Cutoff masses, or completeness limits, of $10^3\ M_\odot$ for the clouds defined by truncation and $2 \times 10^3\ M_\odot$ for those defined by the box method were adopted. As an example, Table 5 shows the numbers and mass distributions of clouds identified by the box method for the various threshold intensities. The table and Figure 12 illustrate that the spectral indices are found to depend only weakly on the method or the threshold intensity. In terms of numbers of clouds identified, the 5 σ threshold seems to best match the set of clouds identified manually. Above the 13 σ (1.5 K) threshold, the number of clouds identified by both methods is less than 10, and the spectral index derived may not be meaningful.

To investigate the sensitivity of the mass spectrum to the spatial resolution, the analyses for the box method were repeated for data sets smoothed to 15′ and 20′ resolution. The threshold intensities were scaled to be the same multiples of the rms noise per channel as for the 10′ resolution data set. The spectral indices were essentially unchanged, within the uncertainties, from what were found using the 10′ resolution data set.

The finding that the spectral index depends only weakly on the method or the threshold intensity is remarkable because the numbers of clouds identified and their masses are much more sensitive to these considerations. One might expect that with increasing smoothing the mass spectrum would tend to harden, as previously distinct clouds are merged into larger clouds. Even this effect is not significant. The findings suggest that the spectral index does decrease with increasing threshold intensity (Table 5), which can be understood if increased thresholds preferentially exclude lower mass clouds, although even this effect is only marginally significant. A best value for α, considering the range of values in Table 5, might be 0.65 ± 0.15.

TABLE 5

PROPERTIES OF THE CLOUD DISTRIBUTION (BOX METHOD)

THRESHOLD		NUMBER OF CLOUDS	MAXIMUM MASS[a]	TOTAL MASS[b]	SPECTRAL
σ	(K)	$>2 \times 10^3\ M_\odot$	($10^5\ M_\odot$)	($10^5\ M_\odot$)	INDEX α
3.....	0.42	33	2.2	7.2	0.78 ± 0.14
5.....	0.70	27	2.2	6.1	0.74 ± 0.14
7.....	0.98	29	2.1	5.0	0.88 ± 0.16
9.....	1.26	22	2.0	4.2	0.81 ± 0.17
11.....	1.54	15	2.0	3.8	0.66 ± 0.17
13.....	1.82	11	2.0	3.5	0.54 ± 0.16
15.....	2.10	11	2.0	3.2	0.60 ± 0.18
17.....	2.39	11	2.0	3.0	0.63 ± 0.19
19.....	2.67	9	2.0	2.8	0.59 ± 0.20
21.....	2.95	7	2.0	2.6	0.50 ± 0.19

[a] Mass of most massive cloud.

[b] Total mass of all clouds with masses $> 10^2\ M_\odot$.

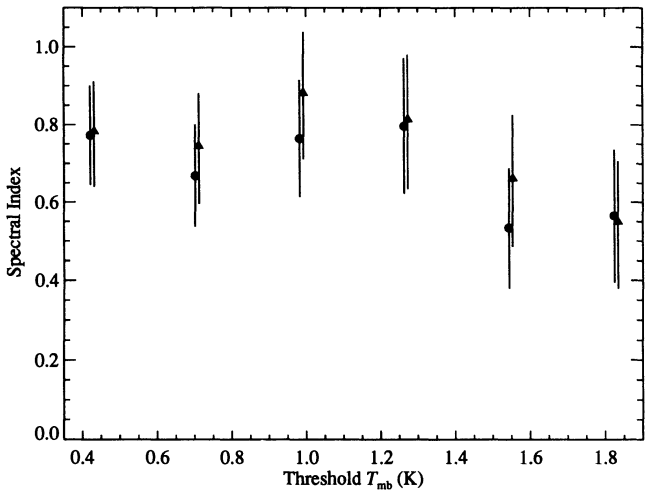

FIG. 12.—Dependence of spectral index for the cumulative mass distribution on threshold intensity for clouds defined by truncation (*circles*) and by the box method (*triangles*). Error bars indicate 1 σ uncertainties. Plotted points are offset slightly for clarity.

The mass spectrum found here is different from that determined using the clouds identified manually and marginally different from most determinations by other workers (Table 4). The steepness of the spectrum for the manually identified clouds might be attributable to the difficulty of resolving the large complex associated with W3 into well-defined clouds. The most massive cloud in the catalog identified by hand has a mass of only $40 \times 10^3 M_\odot$; the automatic methods do not require a simple line profile, and the most massive cloud identified generally has a mass 5 or more times greater (Table 5). Similarly, clouds that are isolated and easily identified are more likely to have lower masses and may therefore be overrepresented in the table of clouds identified by hand. Both effects would steepen the apparent mass spectrum. The spectral index derived from the automatic analyses is greater than those found by others, but not significantly so; the mass spectrum found here for the W3 region may not apply to the Perseus arm in general. The survey covers $\sim$1 kpc at the distance of the Perseus arm, and even this scale may not be large enough to be representative.

REFERENCES

Adler, D. S., Lo, K. Y., Wright, M. C. H., Rydbeck, G., Plante, R. L., & Allen, R. J. 1992, ApJ, 392, 497
Allen, C. 1973, Astrophysical Quantities (London: Athlone), p. 30
Blitz, L., Fich, M., & Stark, A. A. 1982, ApJS, 49, 183
Brand, J., & Blitz, L. 1993, A&A, 275, 67
Bronfman, L., Cohen, R. S., Alvarez, H., May, J., & Thaddeus, P. 1988, ApJ, 324, 248
Campbell, B., Persson, S. E., & McGregor, P. J. 1986, ApJ, 305, 336
Carey, S. J. 1995, Ph.D. thesis, Rensselaer Polytechnic Institute
Casoli, F., Combes, F., & Gerin, M. 1984, A&A, 133, 99
Cohen, R. S., Cong, H., Dame, T. M., & Thaddeus, P. 1980, ApJ, 239, L53
Cohen, R. S., Dame, T. M., & Thaddeus, P. 1986, ApJS, 60, 695
Crawford, D. F., Jauncey, D. L., & Murdoch, H. S. 1970, ApJ, 162, 405
Dame, T. M. 1983, Ph.D. thesis, Columbia Univ.
Dame, T. M., Elmegreen, B. G., Cohen, R. S., & Thaddeus, P. 1986, ApJ, 305, 892
Dame, T. M., et al. 1987, ApJ, 322, 706
de Geus, E. J. 1995, private communication
Digel, S. 1991, Ph.D. thesis, Harvard Univ.
Digel, S., Bally, J., & Thaddeus, P. 1990, ApJ, 357, L29
Digel, S., de Geus, E., & Thaddeus, P. 1994, ApJ, 422, 92
Grabelsky, D. A., Cohen, R. S., Bronfman, L., Thaddeus, P., & May, J. 1987, ApJ, 315, 122
Güsten, R., & Mezger, P. G. 1982, Vistas Astron., 26, 159
Haug, U. 1970, A&AS, 1, 35
Heeschen, D. S. 1951, ApJ, 114, 132
Henderson, A. P., Jackson, P. D., & Kerr, F. J. 1982, ApJ, 263, 116
Humphreys, R. M. 1976, ApJ, 206, 114
———. 1978, ApJS, 38, 309
Infrared Astronomical Satellite (IRAS) Catalogs and Atlases, Vol. 1, Explanatory Supplement, 1988, ed. C. Beichman et al., NASA RP-1190 (Washington, DC: GPO)
Kimeswenger, S., & Weinberger, R. 1989, A&A, 209, 51
Kutner, M. L., & Ulich, B. L. 1981, ApJ, 250, 341
Lada, C. J., Elmegreen, B. G., Cong, H.-I., & Thaddeus, P. 1978, ApJ, 226, L39
Lada, E. A., & Blitz, L. 1988, ApJ, 326, L69
Leung, H. O., & Thaddeus, P. 1992, ApJS, 81, 267
Lo, K. Y., Ball, R., Masson, C. R., Phillips, T. G., Scott, S., & Woody, D. P. 1987, ApJ, 317, L63
Lockman, F. J. 1989, ApJS, 71, 469
Lyder, D. L. 1996, Ph.D. thesis, Univ. Victoria
Mead, K. N., & Kutner, M. L. 1988, ApJ, 330, 399
Morgan, W. W., Sharpless, S., & Osterbrock, D. 1952, AJ, 57, 3
Sanders, D. B., Scoville, N. Z., & Solomon, P. M. 1985, ApJ, 289, 373
Sharpless, S. 1959, ApJS, 4, 257
Snell, R. L., Scoville, N. Z., Sanders, D. B., & Erickson, N. R. 1984, ApJ, 284, 176
Sodroski, T. J. 1991, ApJ, 366, 95
Solomon, P. M., Rivolo, A. R., Barrett, J., & Yahil, A. 1987, ApJ, 319, 730
Solomon, P. M., Sanders, D. B., & Rivolo, A. R. 1985, ApJ, 292, L19
Stark, A. A. 1985, in IAU Symp. 106, The Milky Way Galaxy, ed. H. van Woerden, R. J. Allen, & W. B. Burton (Dordrecht: Reidel), 445
Strong, A. W., et al. 1988, A&A, 207, 1
Thronson, H. A., Lada, C. J., & Hewagama, T. 1985, ApJ, 297, 662
Tilanus, R. P. J., & Allen, R. J. 1989, ApJ, 339, L57
Ungerechts, H., Umbanhowar, P., & Thaddeus, P. 1996, ApJ, submitted
Vogel, S. N., Kulkarni, S. R., & Scoville, N. Z. 1988, Nature, 334, 402
Westerhout, G., & Wendlant, H.-U. 1982, A&AS, 49, 143
Williams, J. P., de Geus, E. J., & Blitz, L. 1994, ApJ, 428, 693
Wouterloot, J. G. A., & Brand, J. 1989, A&AS, 80, 149 (WB)
Wouterloot, J. G. A., Brand, J., Burton, W. B., & Kwee, K. K. 1990, A&A, 230, 21 (WBBK)